Supporting Information

Photo-responsive heterojunction nanosheets of graphene for self-powered flexible devices

Lu Zong,‡[ab] Xiankai Li, ‡[ab] Luting Zhu,‡[a] Xiankai Li,[ab] Jun You,[a] Zehui Li,[d] Hongwei Gao,*[c] Mingjie Li*[a] and Chaoxu Li*[ab]

[a]Group of Biomimetic Smart Materials, Qingdao Institute of Bioenergy and Bioprocess Technology, Chinese Academy of Sciences, Songling Road 189, Qingdao 266101, P. R. China.

[b]Center of Material and Optoelectronics Engineering, University of Chinese Academy of Sciences, 19A Yuquan Road, Beijing 100049, P. R. China.

[c]School of Life Science, Ludong University, Middle Hongqi Road 186, Yantai 264025, P. R. China

[d]State Key Joint Laboratory of Environment Simulation and Pollution Control, School of Environment, Tsinghua University, Shuangqing Road 30, Beijing 100084, P. R. China

‡These authors contributed equally to this work.

*E-mail: gaohongw369@163.com (H. Gao); limj@qibebt.ac.cn (M. Li); licx@qibebt.ac.cn (C. Li).

Supporting experimental section

Electrochemical Characterization: Electrochemical measurements were conducted with a typical three-electrode system on a CHI660E electrochemical workstation (CH Instrument, Shanghai, China) and performed in 6 M KOH solution at room temperature (25 °C). A platinum slice (10 × 10 × 0.1 mm^3) served as the counter electrode, and Hg/HgO electrode as the reference electrode. The working electrode was prepared as follows: the as-prepared inks (0.5 mg mL^{-1}) was coated onto Ni foam (10 × 10 mm^2), dried at 100 °C for 12 h in a vacuum dryer, and then pressed at 10 MPa for 2 min with a tablet press machine to obtain the working electrode. The load of active materials in each working electrode was about 1.0 ± 0.1 mg. Cyclic voltammetry (CV) was measured at different scan rates between −1 and 0 V. The galvanostatic charge-discharge tests were performed at different current densities from 0.5 to 20 A g^{-1} within the same voltage range as CV. Electrochemical impedance spectroscopy (EIS, Nyquist plots) was recorded at open circuit potential superimposed with an amplitude of 10 mV over a frequency range from 10^5 to 0.1 Hz. The gravimetric capacitance for a single electrode C_s (F g^{-1}) was calculated according to the following equation:

$$C=I\Delta t/m\Delta E$$

where I is the discharge current (A), Δt is the discharge time (s), m is the mass of the active material in the working electrode (g) and ΔE is the voltage change excluding the IR drop during the discharge process (V).

For the planar capacitor, CV was measured from 5 to 5000 mV s^{-1}. Galvanostatic charge-discharge test was performed at different current densities from 0.4 to 10 A g^{-1}. EIS measurements were recorded by employing 10 mV amplitude in the frequency range of 10^5 to 0.1 Hz. The areal capacitance for device, C (F cm^{-2}), was calculated according to the following equation:

$$C=I\Delta t/S\Delta E$$

where I is the charge/discharge current (A), Δt is the discharge time (s), S is the area of the device (cm^2) and ΔE is the voltage change excluding the IR drop during the discharge process (V).

Theoretical Calculation: In our work, all spin-polarized plane-wave density functional theory (DFT) calculations were carried out using the DMol module of Materials Studio (MS) 8.0.[S1-S3] We adopt the generalized gradient approximation (GGA) with Perdew−Burke−Ernzerhof (PBE) to describe the exchange and correlation energy, as the functional was proved to be efficient in calculating the GO adsorption[S3-S5]. We employed the basis set, double numerical plus polarization (DNP), to describe the valence orbital of all the atoms. The all-electron relativistic method was applied to treat the core electrons. A smearing width of 0.005 Ha was utilized, which can significantly improve computational performance. When the convergence criteria with respect to the energy, force and displacement (i.e., 1.0×10^{-5} Ha, 2.0×10^{-3} Ha/Å and 5.0×10^{-3} Å) were satisfied, the structure optimization would be considered to be complete. In all calculations, the global orbital cutoff we chose was 5.0 Å and the k-point was 3 × 3 × 1.

For this study, the adsorption energies (E_{ad}) between the GO and MoS_2 is calculated by the following equation:

$$E_{ad} = E_{GO+MoS2} - (E_{GO} + E_{MoS2})$$

where $E_{GO+\ MoS2}$ refers to the total energy of the MoS_2 surface with adsorbed GO; E_{GO} and E_{MoS2} refer to the calculated energies of GO sheet and clean MoS_2 surface respectively. By this definition, a positive E_{ad} value indicates that adsorption process is endothermic and adsorption system is unstable; a negative E_{ad} value indicates that adsorption process is exothermic and adsorption system is stable.

Supporting tables

Table S1 Content of functional groups in GO, MoS_2 on GO, rGO and MoS_2 on rGO by XPS.

GO	Group	C-C/C=C (284.6 eV)	C-O (286.5 eV)	C=O (287 eV)	COOH (288.1 eV)	
	Concentration (%)	60.7	18.8	16.3	4.2	
MoS_2 on GO	Group	C-C/C=C (284.5 eV)	C-O (286.4 eV)	C=O (286.9 eV)	COOH (287.9 eV)	
	Concentration (%)	64.3	18	14.4	3.2	
rGO	Group	C-C/C=C (284.7 eV)	C-O (286.5 eV)	C=O (288 eV)	C(O)O (289.2 eV)	C-N (285.7 eV)
	Concentration (%)	74.3	7.2	4.3	1.9	8.4
MoS_2 on rGO	Group	C-C/C=C (284.6 eV)	C-O (286.2 eV)	C=O (287.8 eV)	C(O)O (289.1 eV)	C-N (285.5 eV)
	Concentration (%)	77.2	8.0	2.8	1.2	9.7

73 **Table S2** Comparison of electrochemical performance with other planar supercapacitors.

Electrode	Power density (mW cm^{-2})	Energy density (mWh cm^{-2})	Reference
rGO	0.0090	0.014	S6
rGO quantum dots	0.0075	0.074	S7
rGO/Poly(3,4-ethylenedioxythiophene)	0.020	0.0068	S6
rGO/carbon nanotube	0.050	0.0038	S8
titanium carbide nanosheet	0.045	0.0030	S9
rGO/Mo	0.075	0.00022	S10
TiN/CNT	0.097	0.0027	S11
rGO/polypyrrole/MnO_2	1.3	0.0092	S12
MoS_2 on rGO	0.20	0.053	This study

Supporting figures

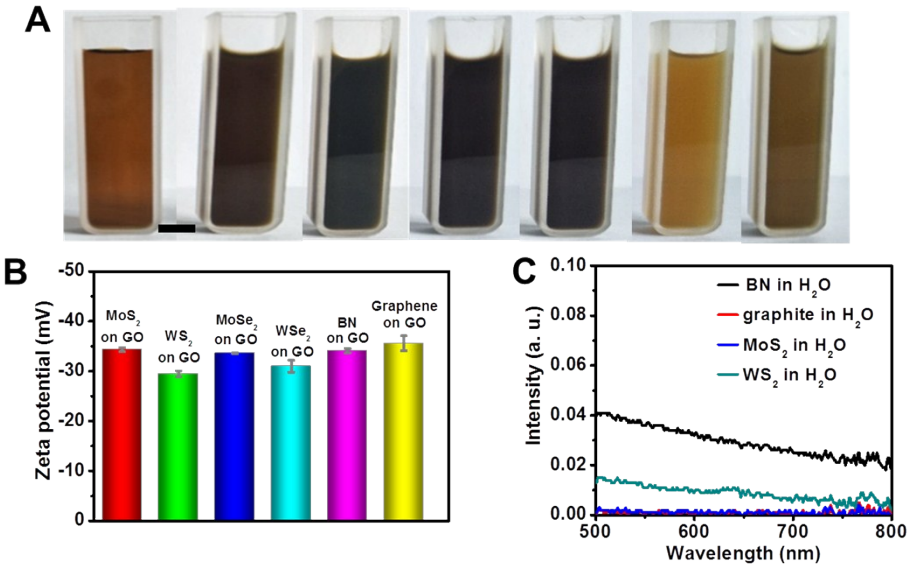

Fig. S1 (A & B) Visual observations (A) and Zeta potential values (B) of exfoliated solution: GO, MoS_2 on GO, WS_2 on GO, $MoSe_2$ on GO, WSe_2 on GO, BN on GO and graphene on GO (From left to right). Scale bar is 5 mm. (C) UV–vis spectra of exfoliated 2D nanomaterials without GO.

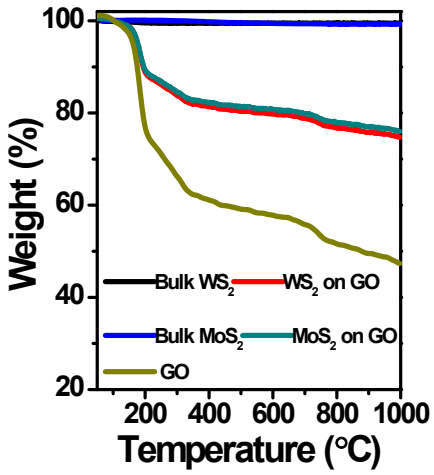

Fig. S2 Thermogravimetric analysis (TGA) of GO, TMDs and their heterogeneous structures at a heating rate of 20 ºC min^{-1} under 40 mL min^{-1} N_2 flow. The TMDs concentration was evaluated by TGA according to a simple addition rule. Sample was produced by using GO (O/C 64.7 atm%) concentration 1 mg mL^{-1} and initial MoS_2 dosage 0.5 wt% at *pH* 10 and for exfoliation time 60 h.

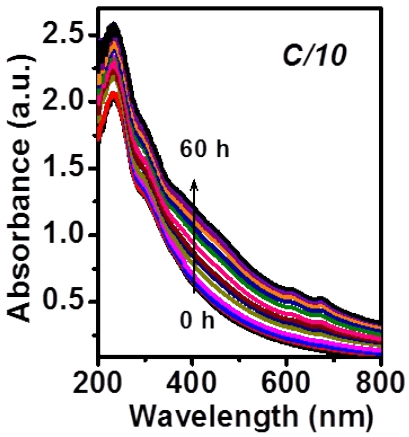

87

88 **Fig. S3** UV–vis spectra of exfoliated MoS_2 produced in 1 mg mL^{-1} GO solution for different
89 sonication time. Absorption peaks are located at ~670 nm. Experimental parameters: GO
90 (O/C 64.7 atm%) concentration 1 mg mL^{-1}; initial MoS_2 dosage 0.5 wt%; *pH* 10. *C/10* refers
91 to suspension dilution up to 10 times for UV−vis analysis.

92

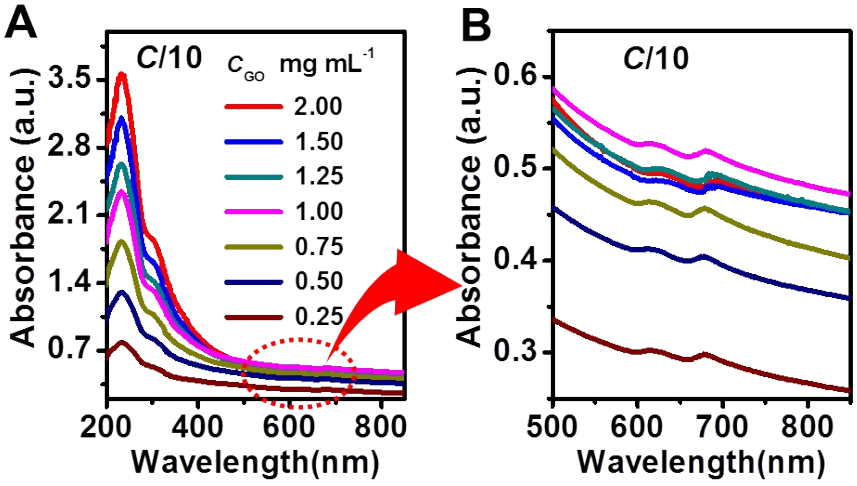

93

94 **Fig. S4** Influence of GO concentrations on UV–vis spectra of exfoliated MoS_2 produced at
95 different GO (O/C 64.7 atm%) concentrations. (A) Wavelength of 200~850 nm. (B)
96 Wavelength of 500~850 nm. Initial MoS_2 dosage 0.5 wt%; *pH* 10; exfoliation time 60 h. *C/10*
97 refers to suspension dilution up to 10 times for UV−vis analysis.

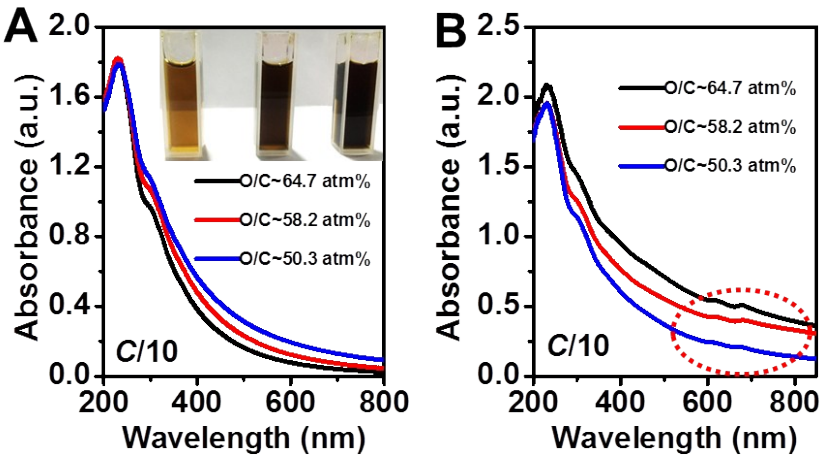

Fig. S5 (A) UV−vis spectra of GO solution with different contents of O-containing groups. (B) UV–vis spectra of MoS_2 exfoliated in solution of GO with different contents of O-containing groups. GO concentration: 1 mg mL^{-1}; Initial MoS_2 dosage: 0.5 wt%; *pH* 10; Exfoliation time: 60 h. *C/10* refers to suspension dilution up to 10 times for UV−vis analysis.

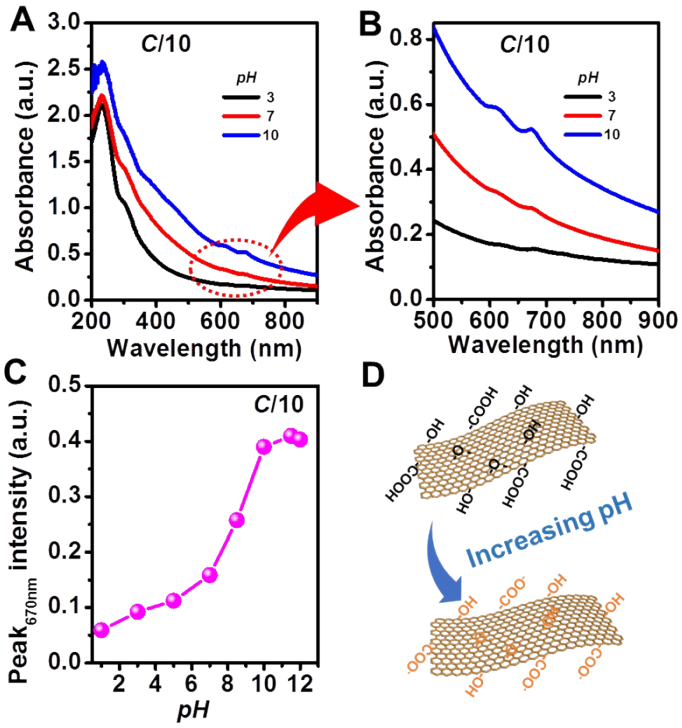

106

107 **Fig. S6** (A-B) UV–vis spectra of MoS_2 exfoliated in GO solution at different *pH* values. (C)

108 Dependence of UV–vis absorption at 670 nm of exfoliated MoS_2 on pH in GO solution. (D)

109 Schematic illustration of ionic GO at basic pH values. At higher pH values, ionized oxygen

110 species increased the GO dispersibility, and facilitated adsorption of MoS_2 on GO.[S13] GO:

111 O/C 64.7 atm%; GO concentration: 1 mg mL^{-1}; Initial MoS_2 dosage: 0.5 wt%; Exfoliation

112 time: 60 h. *C/10* refers to suspension dilution up to 10 times for UV−vis analysis.

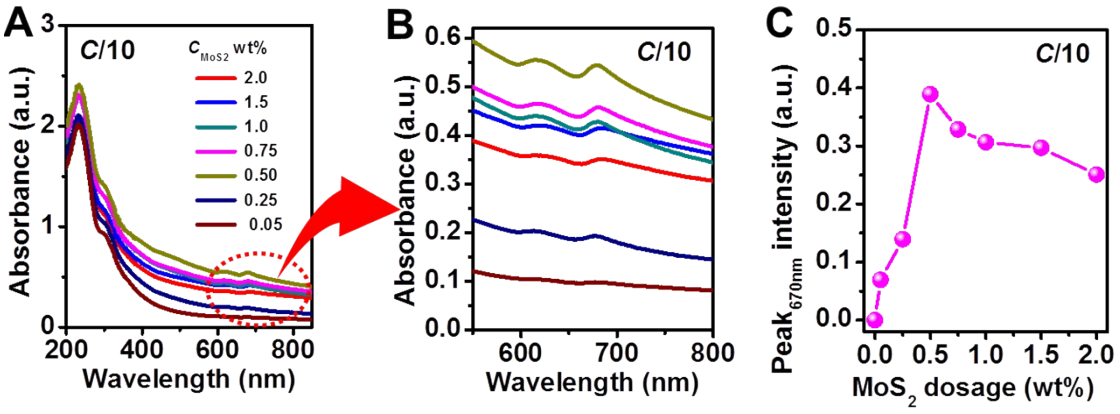

114

115 **Fig. S7** (A & B) UV–vis spectra of MoS_2 exfoliated with at different dosages of bulk MoS_2.

116 (C) Dependence of UV–vis absorption at 670 nm of exfoliated MoS_2 on different dosages of

117 bulk MoS_2. GO: O/C 64.7 atm%; GO concentration: 1 mg mL^{-1}; *pH* 10; Exfoliation time: 60

118 h. *C/10* refers to suspension dilution up to 10 times for UV−vis analysis.

119

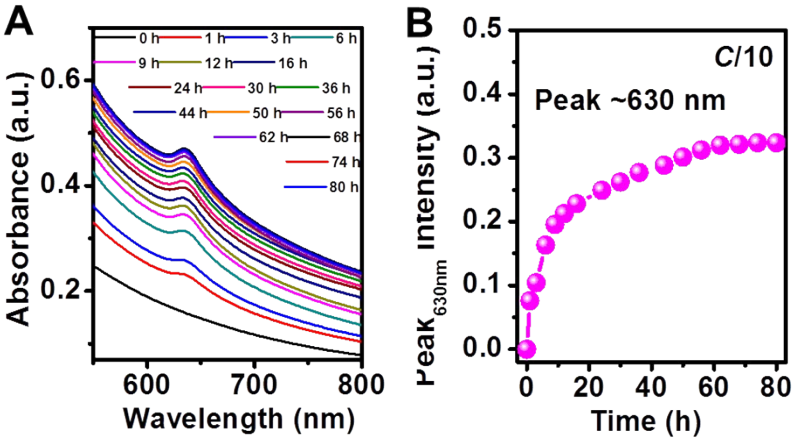

120

121 **Fig. S8** (A) UV–vis spectra of WS_2 exfoliated in GO solution with different ultrasonication

122 time. (B) Dependence of UV–vis absorption at 630 nm of exfoliated WS_2 on different

123 ultrasonication time. GO: O/C 64.7 atm%; GO concentration: 1 mg mL^{-1}; *pH* 10; Initial WS_2

124 dosage: 1 wt%. *C/10* refers to suspension dilution up to 10 times for UV−vis analysis.

125

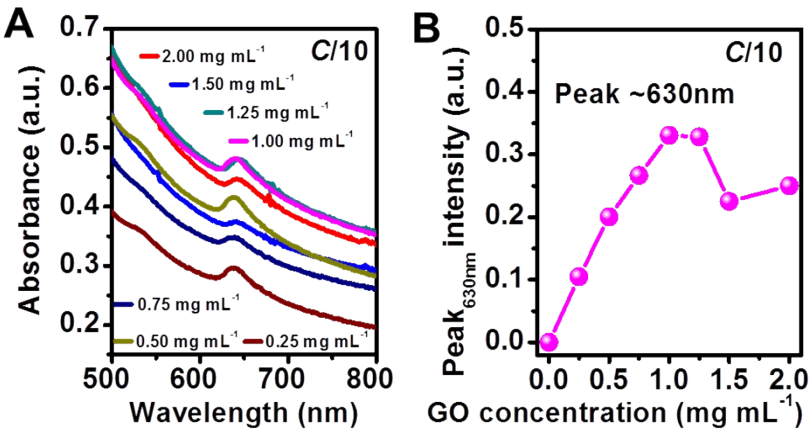

126

127 **Fig. S9** (A) Influence of GO concentrations on UV–vis spectra of exfoliated WS_2 produced at
128 different GO (O/C 64.7 atm%) concentrations. (B) Dependence of UV–vis absorption at 630
129 nm of exfoliated WS_2 on different GO (O/C 64.7 atm%) concentrations. Initial WS_2 dosage: 1
130 wt%; *pH* 10; Exfoliation time: 60 h.

131

132

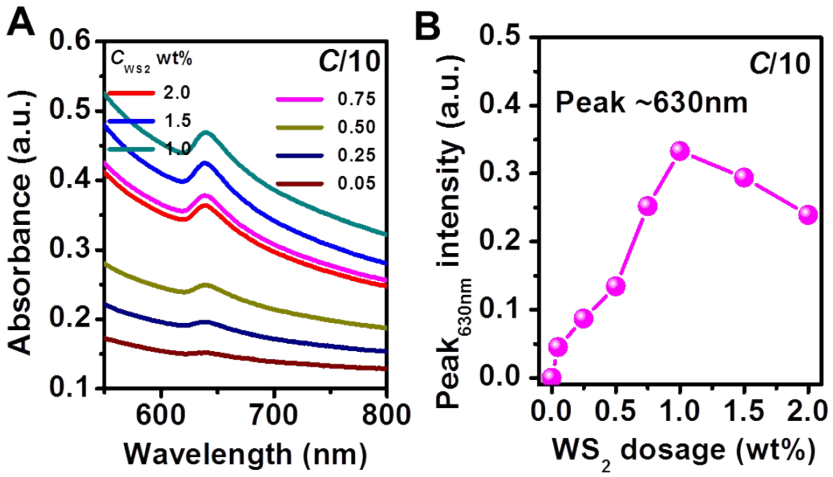

133

134 **Fig. S10** (A) UV–vis spectra of WS_2 exfoliated with at different dosages of bulk WS_2. (B)
135 Dependence of UV–vis absorption at 630 nm of exfoliated WS_2 on dosages of bulk WS_2. GO:
136 O/C 64.7 atm%; GO concentration: 1 mg mL^{-1}; *pH* 10; Exfoliation time: 60 h.

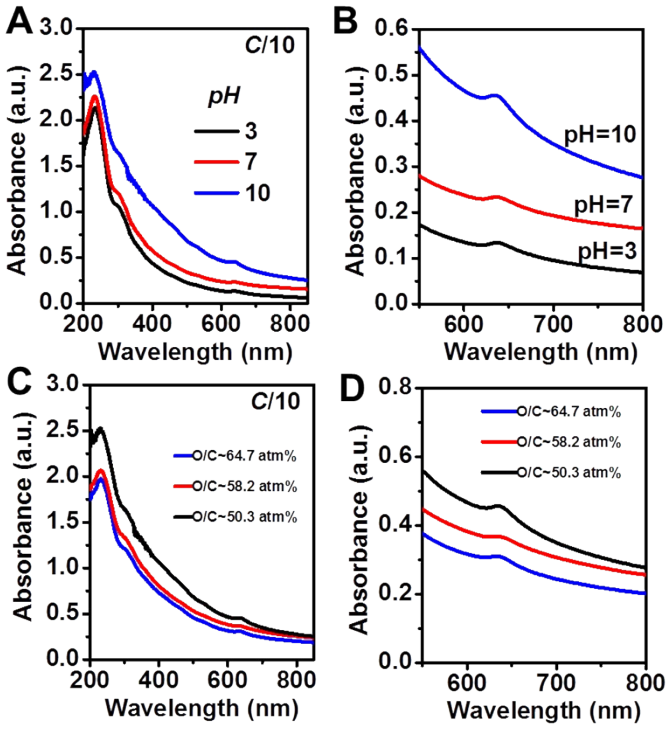

137

138 **Fig. S11** (A-B) UV–vis spectra of WS_2 exfoliated in GO solution at different *pH* values. GO:
139 O/C 64.7 atm%; GO concentration: 1 mg mL^{-1}; Initial WS_2 dosage: 1 wt%; Exfoliation time:
140 60 h. (C-D) UV–vis spectra of WS_2 exfoliated in solution of GO with different contents of O-
141 containing groups. GO concentration: 1 mg mL^{-1}; Initial WS_2 dosage: 1 wt%; *pH* 10;
142 Exfoliation time 60 h.

143

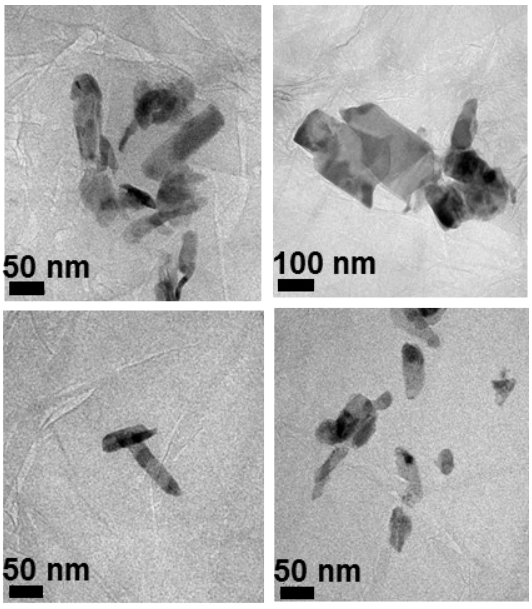

144

145 **Fig. S12** Typical TEM images of heterojunction nanosheets of MoS_2 on GO nanosheets.

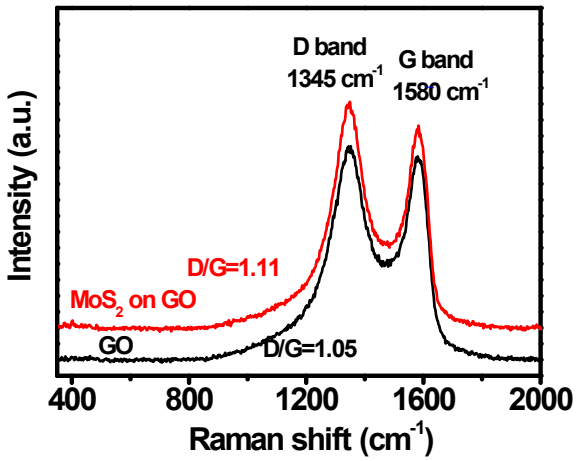

Fig. S13 Raman spectra of GO and heterojunction nanosheets of MoS_2 on GO.

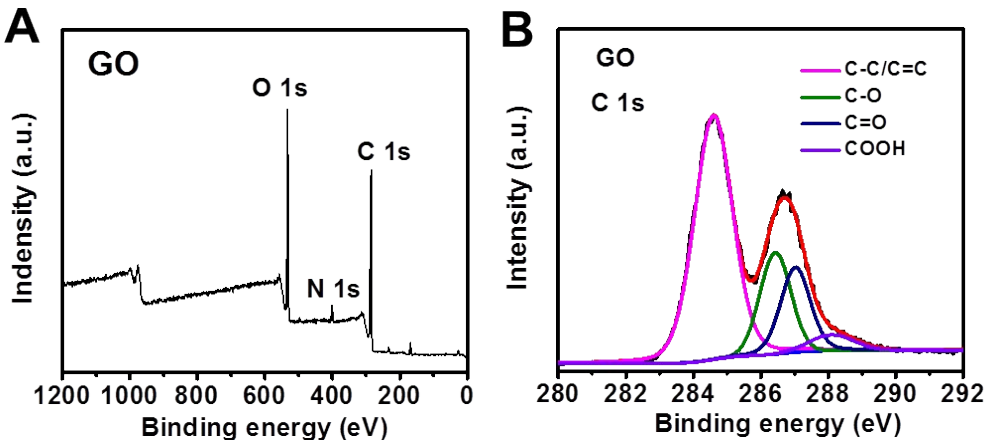

Fig. S14 XPS spectra of GO. Wide-scan survey (A) and C1s XPS spectra (B).

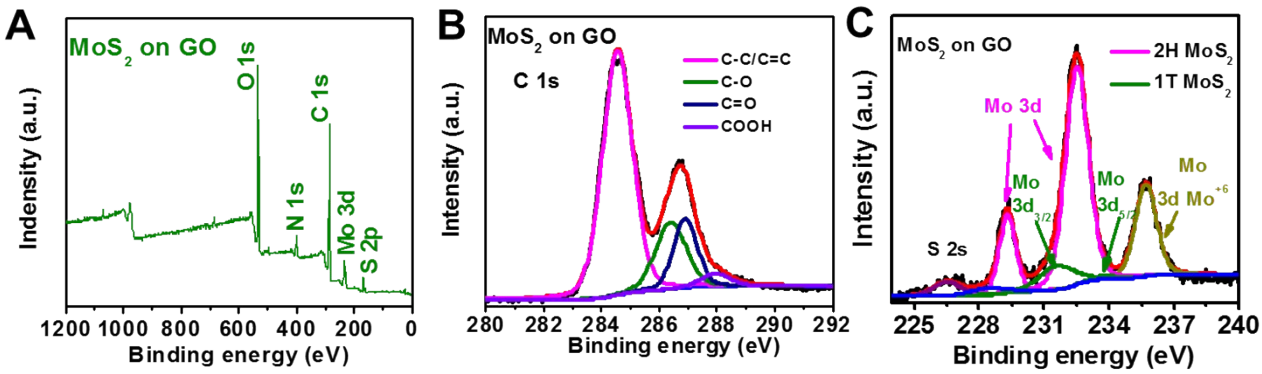

156

157 **Fig. S15** XPS spectra of heterojunction of heterojunction nanosheets of MoS_2 on GO. (A)

158 Wide-scan survey. (B) C1s. (C) Mo3d/S2s.

159

160

161

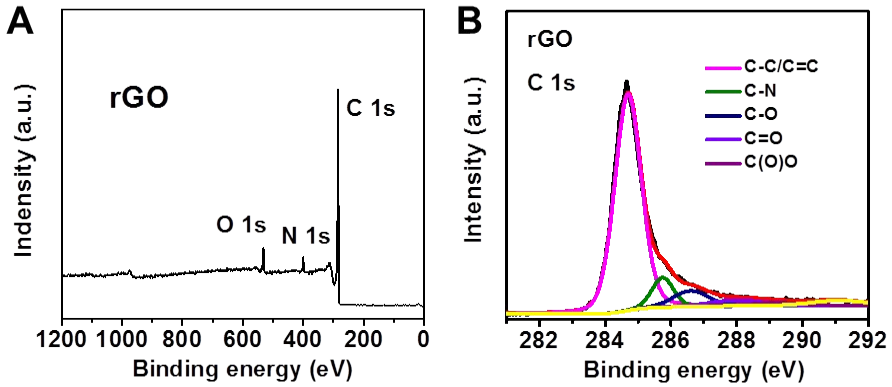

162

163 **Fig. S16** XPS spectra of rGO. (A) Wide-scan survey. (B) C1s XPS spectra.

164

165

166

167

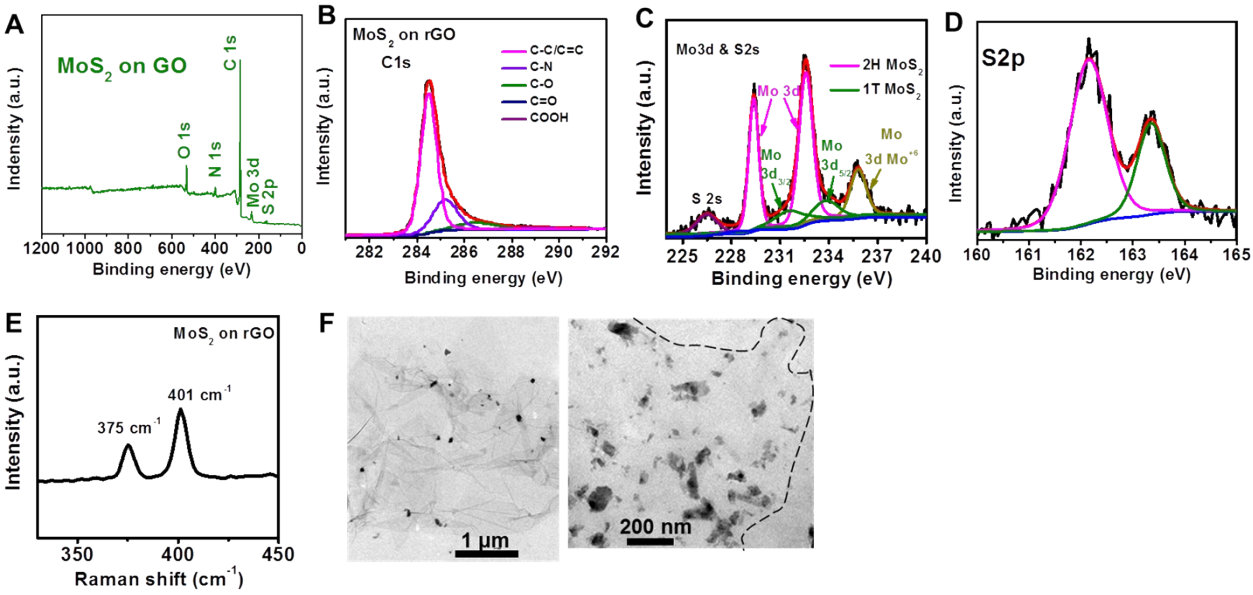

168

169 **Fig. S17** XPS spectra of heterojunction of heterojunction nanosheets of MoS_2 on rGO. (A)

170 Wide-scan survey, (B) C1s, (C) Mo3d/S2s and (D) S2p. (E & F) Raman spectrum (E) and

171 TEM images (F) of MoS_2 on rGO.

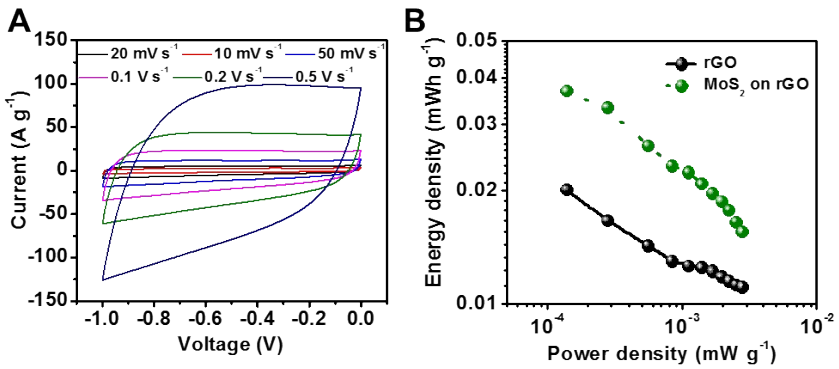

173

174 **Fig. S18** Electrochemical tests of heterojunction nanosheets of MoS_2 on rGO in three-
175 electrode system. (A) Cyclic voltammograms at different scan rates. (B) Ragone plots. rGO
176 was given for comparison.

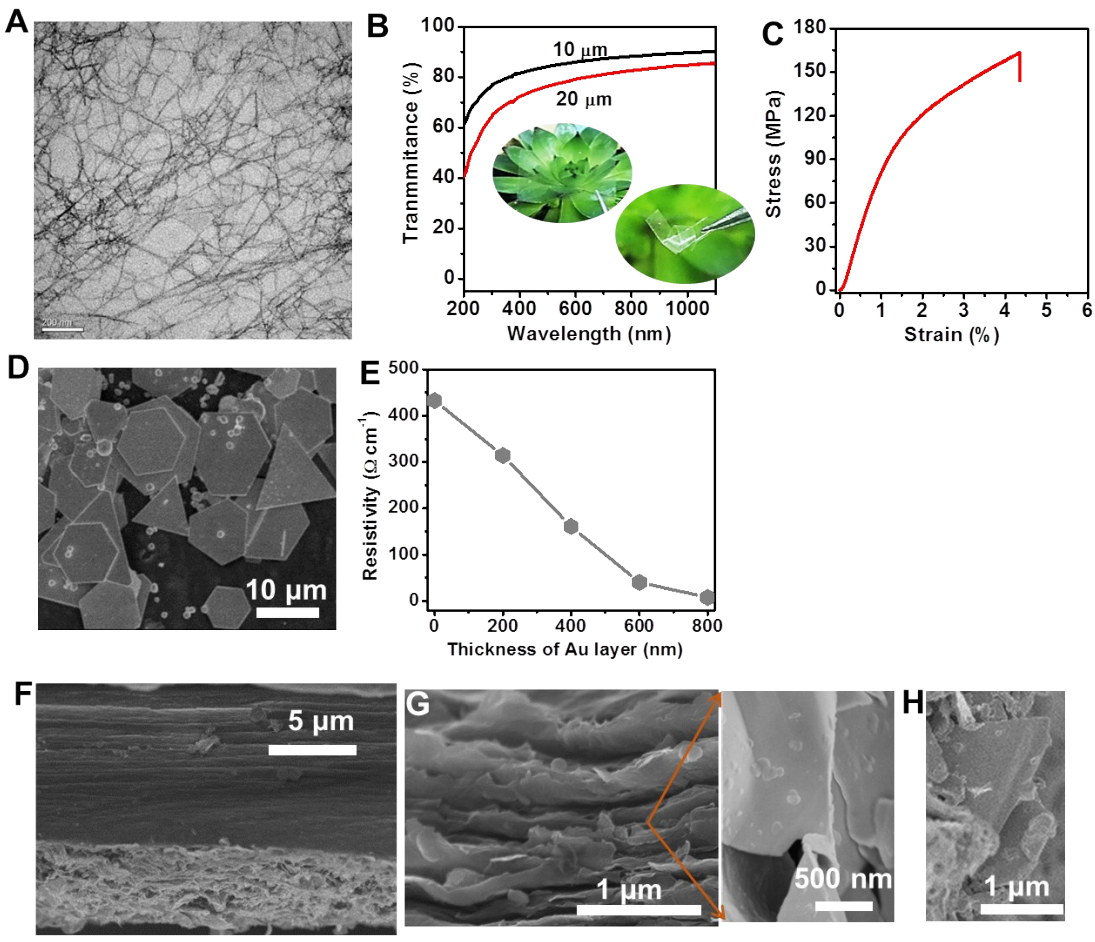

Fig. S19 (A) TEM image of CNFs. (B) Light transmittance (%) of CNFs film with different thicknesses. Inset shows photographs of flexible and transparent CNF film (10 μm in thickness). (C) Stress–strain curve of CNFs film. (D) SEM image of Au microflakes. (E) Resistivity *vs* thickness of Au layer. (F-H) Cross-section SEM images of the capacitor: three distinct layers of cellulose, heterojunction nanosheets and Au flakes (F), heterojunction nanosheets layer with nacre-like structure (B) and Au flakes (C).

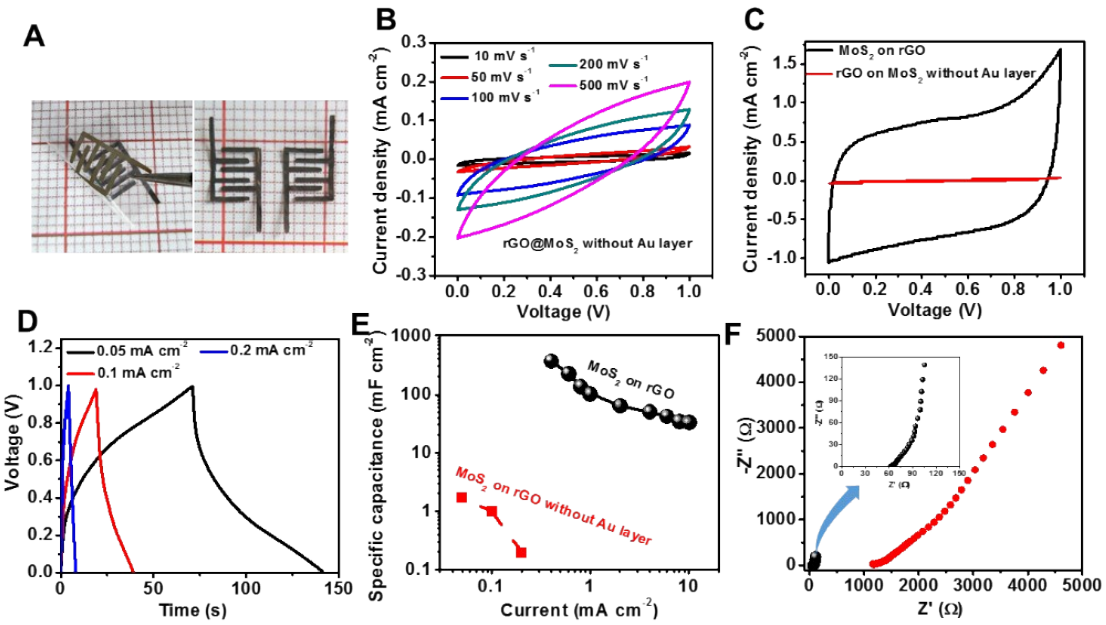

186

187 **Fig. S20** (A & B) Planar capacitor without Au layer: Flexibility and stability demonstration
188 (A) and CV curves of at different scan rates of 5−500 mV s^{-1} (B). (C-F) Electrochemical tests
189 of planar capacitor based on heterojunction nanosheets of MoS_2 on rGO: CV curves at 50 mV
190 s^{-1} (C), Galvanostatic charge–discharge curves at different current densities (D), Ragone plots
191 (E) and Nyquist plots (F). Planar capacitor without Au layer was tested as control.

192

193

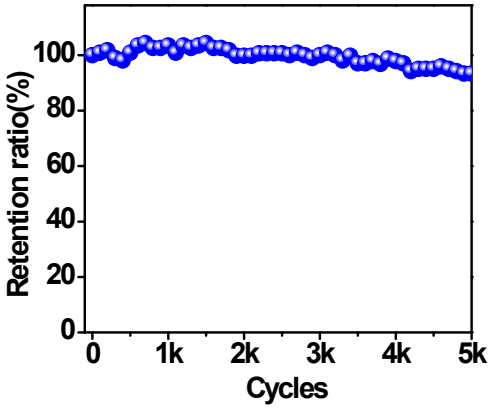

194

195 **Fig. S21** Capacitance retention of as-prepared planar capacitor under long-term
196 charge−discharge cycles.

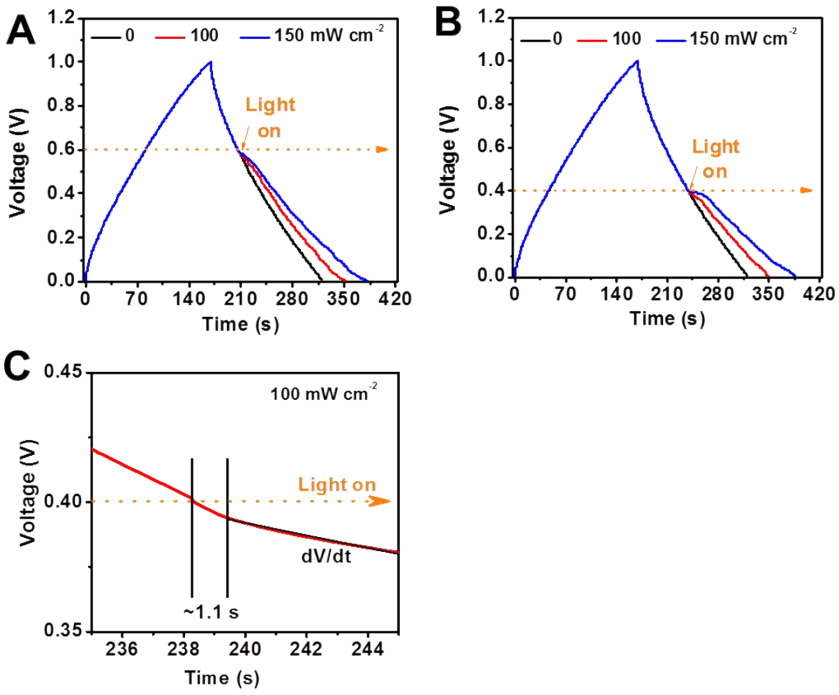

197

198 **Fig. S22** Charge–discharge curve (1 mA cm^{-2}) under continuous NIR irradiation with

199 different photo intensities starting at 0.6 V (A) and 0.4 V (B). (C) Zoom-in curve of (B).

200

201

202

203

204

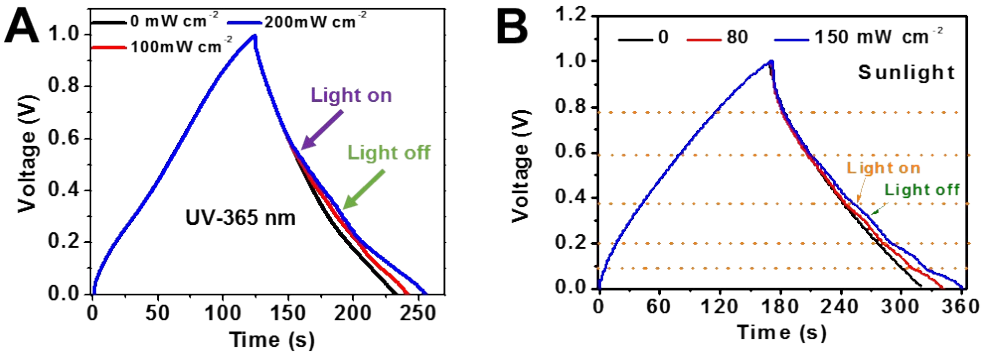

205

206 **Fig. S23** Charge–discharge curve (1 mA cm^{-2}) under periodic UV (A) and sunlight (B)

207 irradiation with different photo intensities.

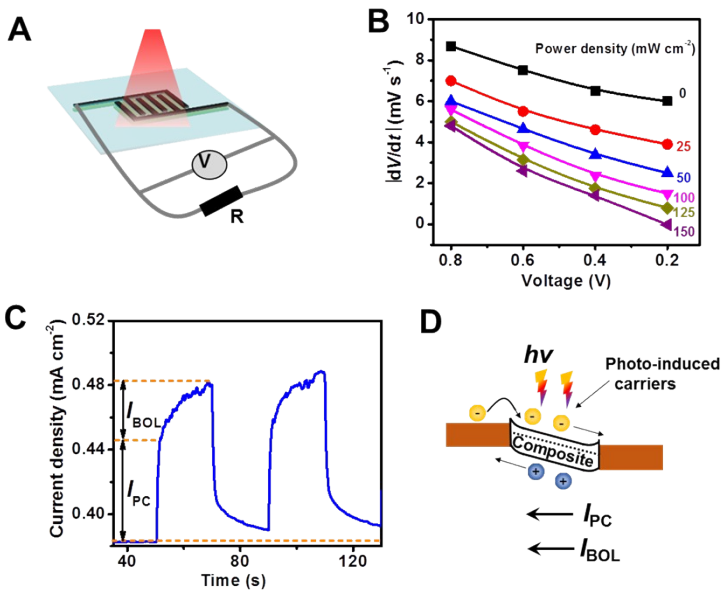

209

210 **Fig. S24** (A) Schematic illustration of setup. (B) Dependence of estimated discharge rate
211 ($|dV/dt|$) on light intensity at different different NIR intensities. (C) Photoconduction (I_{PC}) and
212 bolometric photocurrent (I_{BOL}). (D) Suggested schematic illustration of the photoelectric
213 responsivity of the hybrid nanosheets.

214

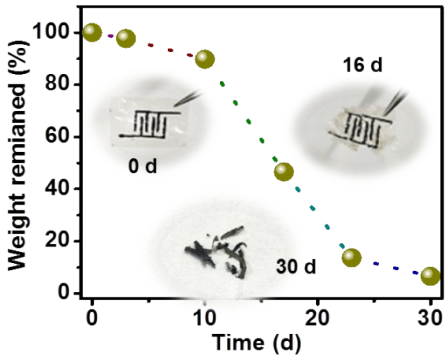

215

216 **Fig. S25** Time dependence of weight loss for biodegradation of capacitor in soil. The inset
217 gives visual observations after different degradation periods. To perform the biodegradation
218 test, the capacitor was buried in natural soil at 2 cm depth. At designed interval, the degraded
219 sample was excavated out, cleaned carefully with ethanol, and then dried under 50 °C for 2 h.
220 The sample with degradation time from 0 to 30 days was characterized with the mass change
221 for the degradation kinetics.

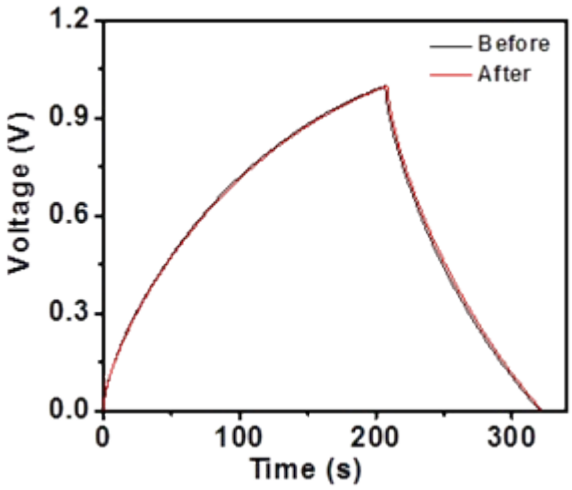

223

224 **Fig. S26** Galvanostatic charge–discharge curves after vapor permeability and successively
225 balanced in air condition (25 °C; Humidity 25%) for one day. Punched CNFs film (Mesh
226 number~100, pore size~0.2 mm).

227

228

229

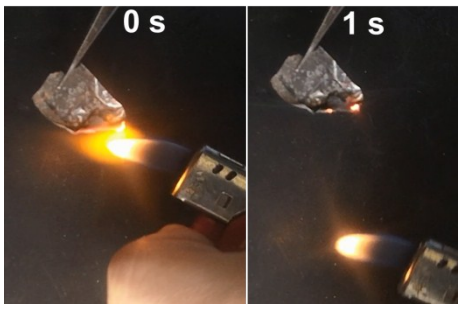

230

231 **Fig. S27** Optical images of the soft capacitor on flaming fire (Left) and away from the fire
232 (Right).

Supporting references:

S1. B. Delley, *J. Chem. Phys.*, 1990, **92**, 508-517.

S2. B. Delley, *J. Chem. Phys.*, 2000, **113**, 7756-7764.

S3. Z. W. Huang, Z. J. Li, Q. Y. Wu, L. R. Zheng, L. M. Zhou, Z. F. Chai, X. L. Wang and W. Q. Shi, *Environ. Sci.-Nano*, 2018, **5**, 2077-2087.

S4. C. C. Chang, C. Y. Liu, S. Y. Wu and M. K. Tsai, *Phys. Chem. Chem. Phys.*, 2017, **19**, 4989-4996.

S5. H. S. Moon, J. H. Lee, S. Kwon, I. T. Kim and S. G. Lee, *Carbon Lett.*, 2015, **16**, 116-120.

S6. G. Qu, J. Cheng, X. Li, D. Yuan, P. Chen, X. Chen, B. Wang and H. Peng, *Adv. Mater.*, 2016, **28**, 3646-3652.

S7. W. W. Liu, Y. Q. Feng, X. B. Yan, J. T. Chen and Q. J. Xue, *Adv. Funct. Mater.*, 2013, **23**, 4111-4122.

S8. L. Kou, T. Huang, B. Zheng, Y. Han, X. Zhao, K. Gopalsamy, H. Sun and C. Gao, *Nat. Commun.*, 2014, **5**, 3754.

S9. C. J. Zhang, M. P. Kremer, A. Seral-Ascaso, S. H. Park, N. McEvoy, B. Anasori, Y. Gogotsi and V. Nicolosi, *Adv. Funct. Mater.*, 2018, **28**, 1705506.

S10. G. Lee, S. K. Kang, S. M. Won, P. Gutruf, Y. R. Jeong, J. Koo, S. S. Lee, J. A. Rogers and J. S. Ha, *Adv. Energy Mater.*, 2017, **7**, 1700157.

S11. P. Sun, R. Lin, Z. Wang, M. Qiu, Z. Chai, B. Zhang, H. Meng, S. Tan, C. Zhao and W. Mai, *Nano Energy*, 2017, **31**, 432-440.

S12. Y. Huang, H. Hu, Y. Huang, M. Zhu, W. Meng, C. Liu, Z. Pei, C. Hao, Z. Wang and C. Zhi, *ACS Nano*, 2015, **9**, 4766-4775.

S13. B. Konkena and S. Vasudevan, *J. Phys. Chem. Lett.*, 2012, **3**, 867-872.